Quantum spin Hall insulator with a large bandgap, Dirac fermions, and bilayer graphene analog

Sergey S. Krishtopenko, Frederic Teppe

CONDENSED MATTER PHYSICS

Quantum spin Hall insulator with a large bandgap, Dirac fermions, and bilayer graphene analog

Sergey S. Krishtopenko[1,2] and Frédéric Teppe[1]*

The search for room temperature quantum spin Hall insulators (QSHIs) based on widely available materials and a controlled manufacturing process is one of the major challenges of today's topological physics. We propose a new class of semiconductor systems based on multilayer broken-gap quantum wells, in which the QSHI gap reaches 60 meV and remains insensitive to temperature. Depending on their layer thicknesses and geometry, these novel structures also host a graphene-like phase and a bilayer graphene analog. Our theoretical results significantly extend the application potential of topological materials based on III–V semiconductors.

INTRODUCTION

Quantum spin Hall insulators (QSHIs), also known as two-dimensional (2D) topological insulators, are characterized by a bulk bandgap and gapless helical edge channels (*1*, *2*) protected from backscattering by time-reversal symmetry. This fascinating new quantum phase of matter suggests, among others, the design of groundbreaking electronic devices with dissipationless spin currents and the realization of Majorana bound states at the interface with superconductors (*3*, *4*). In this context, QSHI materials with controlled growth and technological processing are in great demand. In addition, a sufficiently large bulk gap is required to overcome the current constraint of cryogenic temperature operation and the problem of short coherence length of the edge channels. Despite numerous theoretical predictions of a QSHI state in a large number of thin films and 2D materials (*5*–*9*), its inherent characteristic—a quantum spin Hall effect (*10*) with its universal quantized conductance—has been experimentally established by a direct transport measurement only in inverted HgTe quantum wells (QWs) (*11*) and broken-gap InAs/GaSb QW bilayers (*12*, *13*).

In HgTe QWs, the inverted band structure responsible for the QSHI state is due to the strong spin-orbit interaction in the HgTe layer. The position of the electron- and hole-like subbands therefore depends on the QW width in such a way that QWs wider than a critical value d_c have inverted subbands (*14*), whereas QWs thinner than d_c have a non-inverted band ordering and feature a trivial band insulator (BI) state. At the critical thickness, HgTe QWs experience a topological phase transition and host a single-valley spin-degenerate Dirac cone at the Γ point of the Brillouin zone (*15*). The maximum bulk gap achievable in inverted HgTe QWs grown on CdTe does not exceed 16 meV, but a gap of 60 meV was recently reached (*16*) in compressively strained HgTe QWs. However, this large gap is only available at low temperatures, whereas increasing of temperature induces the gap closing and phase transition into trivial state (*17*, *18*). The latter is caused by strong temperature dependence of the energy of the Γ_6 bulk band in HgCdTe materials (*19*). However, the high-quality HgTe-based QSHIs grown by molecular beam epitaxy (MBE) are not widely accessible. We also note that the weak bonding between Hg and Te makes these toxic species highly volatile and hazardous during processing.

Although InAs/GaSb broken-gap QWs are also made of toxic compounds, their bonds are stronger than those of HgTe, and the material is therefore stable and less dangerous. In addition, these MBE-grown III–V semiconductors having a controlled technological process are accessible worldwide. However, the bulk gap in inverted InAs/GaSb QW bilayers is much smaller (*12*) than that in HgTe QWs. The band inversion in these broken-gap structures embedded between AlSb barriers results from the fact that the valence band edge of GaSb is higher than the conduction band edge of the InAs layer. Because the InAs/GaSb QW bilayer does not have inversion symmetry in the growth direction, the crossing of electron- and hole-like subbands arises away from the Γ point of the Brillouin zone (*20*). Because these levels are mixed at nonzero quasi-momentum **k**, the band inversion opens a hybridization gap of a few millielectron volts in the QW bilayer.

Since the first experimental demonstration of the QSHI state in the InAs/GaSb QW bilayers, some attempts have been made to overcome the problem of the small inverted bandgap (*13*). Lately, its value has been enhanced by replacing the GaSb layer of the composite QW with a GaInSb alloy. However, the maximum value reached in this way was only on the order of 20 meV (*21*). Thus, the InAs/Ga(In)Sb QW bilayers seem to be less favorable for potential applications in topological electronics than the HgTe-based QWs, despite their many previously mentioned benefits and their promising physical properties, including a good interface with superconductors (*22*, *23*) and an in situ electric tunability (*24*). Besides the hybridization gap opening at nonzero **k**, another consequence of the structure inversion asymmetry in the InAs/GaSb QW bilayers is that unlike HgTe QWs, they do not feature a Dirac cone across topological phase transitions.

Here, we introduce a new class of multilayer InAs/GaSb QWs, which differ from conventional QW bilayers by their band crossing at the center of the Brillouin zone. To eliminate the structure inversion asymmetry, we attach an additional InAs or GaSb layer to the InAs/GaSb QW bilayer. We now define that the novel three-layer InAs/GaSb QWs have an "InAs geometry" or a "GaSb geometry" if they contain two symmetrical layers of InAs or GaSb, respectively. First, we show that the phase transitions in the QWs with InAs geometry are similar to those of HgTe/CdTe QWs. In particular, depending on the layer thicknesses, our structures allow the realization of massless Dirac fermions, semimetal (SM), and a QSHI state with a maximum gap of 16 meV. Second, we show that the QWs with GaSb geometry partially hold the properties of two tunnel-coupled HgTe QWs (*25*), such as the specific band spectrum of graphene bilayer, its "unconventional" quantum Hall effect (*26*), and its electrically tunable bandgap. Finally, we reveal that strain engineering of the three InAs/GaInSb QWs with InAs geometry allows the realization of a QSHI with a bandgap greater than 60 meV, comparable to that of strained HgTe QWs (*16*), but nearly insensitive to temperature.

[1]Laboratoire Charles Coulomb (L2C), UMR CNRS 5221, University of Montpellier, 34095 Montpellier, France. [2]Institute for Physics of Microstructures, Russian Academy of Sciences, GSP-105, 603950 Nizhny Novgorod, Russia.
*Corresponding author. Email: frederic.teppe@umontpellier.fr

RESULTS

Three-layer InAs/GaSb QWs with InAs geometry

Phase diagram

We first consider symmetrical InAs/GaSb/InAs QWs confined by outer AlSb barriers. The QW is supposed to be grown on (001) GaSb buffer. Because the electron-like subbands are localized in the InAs layers, whereas the hole-like subbands are localized in the GaSb layers, the InAs/GaSb/InAs QWs can be contingently considered as "double QW for electrons" with a GaSb middle barrier, which also plays a role of "QW for holes" (Fig. 1A). Figure 1B shows positions of electron-like ($E1$ and $E2$) and hole-like ($H1$) subbands at zero quasi-momentum $\mathbf{k}$ as a function of InAs-layer thickness d_1 for GaSb-layer thickness of d_2 = 4 nm. In this case, it is intuitively clear that the electron-like levels $E1$ and $E2$ are connected with even-odd state splitting, arising from the tunnel-coupled "QWs for electrons". If InAs layers are thin ($d_1 < d_{1c}$, where d_{1c} depends on d_2), the $E1$ and $E2$ subbands lie above the hole-like subbands, and the three-layer QW has a trivial band ordering. For $d_1 > d_{1c}$, the $E1$ subband lies below the $H1$ level, and the QW is characterized by inverted band structure.

In Fig. 1C, we provide a phase diagram for the QWs of InAs geometry with different layer thicknesses. Typical band dispersions for each phase are shown in the bottom panels. In the diagram, the solid curve describing the crossing between $E1$ and $H1$ subbands divides the d_1-d_2 plane into a white region, corresponding to trivial BI phase with direct band ordering, and a gray region with inverted band structure. The gray region, in its turn, is split into open and striped areas, corresponding to QSHI state and SM, respectively. As shown in Fig. 1F, the SM phase is characterized by a vanishing indirect bandgap when the side maxima of the valence subband exceed in energy the conduction subband bottom. We note that the QWs grown along (001) direction positions of the side maxima in the valence band are independent of d_1 and d_2 and always lie along (110), ($\bar{1}$10), (1$\bar{1}$0), and ($\bar{1}\,\bar{1}$0) crystallographic directions. Thus, by varying the layer thicknesses in the QW with InAs geometry, one can realize BI, QSHI, or SM phases.

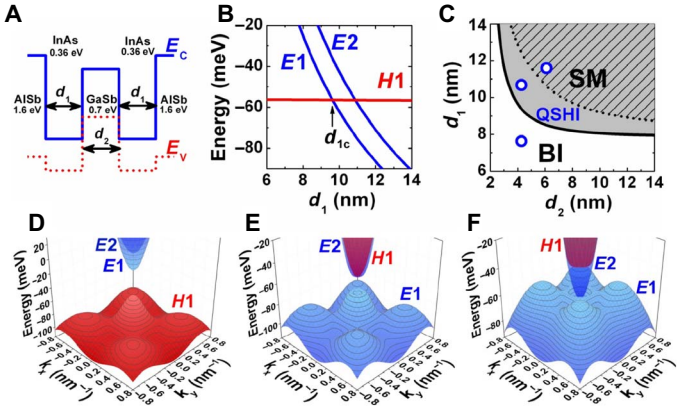

Fig. 1. Band structure of three-layer InAs/GaSb QWs with InAs geometry. (**A**) Schematic representation of symmetrical three-layer InAs/GaSb QWs with InAs geometry. The numbers show the bandgap values in materials of the layers. Here, d_1 and d_2 are the thicknesses of InAs and GaSb layers, respectively. The QW is supposed to be grown on (001) GaSb buffer. (**B**) Energy of electron-like (blue curves) and heavy hole–like (red line) subbands at $\mathbf{k}$ = 0, as a function of d_1 at d_2 = 4 nm. Zero energy corresponds to the top of the valence band in bulk GaSb. (**C**) Phase diagram for different d_1 and d_2. The white open region is a BI phase, whereas the gray-striped region defines an SM phase. The gray open region corresponds to the QSHI state. (**D** to **F**) 3D plot of the band structure at BI (D), QSHI (E), and SM (F) phases. The x and y axes are oriented along (100) and (010) crystallographic directions, respectively. The thicknesses of the layers for each phase, used in the calculations, are marked in (C) by blue open symbols.

To describe a quantum phase transition between BI and QSHI states, we derive effective a 2D Hamiltonian valid for the states in the vicinity of the Γ point. Distinct from HgTe/CdTe QWs (*2*), we take into account additional $E2$ subband, lying close in energy to the $E1$ and $H1$ states. In the basis set $|E1,+\rangle$, $|H1,+\rangle$, $|E2,-\rangle$, $|E1,-\rangle$, $|H1,-\rangle$, and $|E2,+\rangle$, the 2D Hamiltonian for the QW of InAs geometry has the form

$$H_{\mathrm{InAs}}(k_x, k_y) = \begin{pmatrix} H_1(k_x, k_y) & 0 \\ 0 & H_1^*(-k_x, -k_y) \end{pmatrix} \quad (1)$$

where the asterisk stands for complex conjugation, k_x and k_y are momentum $\mathbf{k}$ components in the plane, $k_\pm = k_x \pm ik_y$, and $H_1(k_x, k_y)$ is written as

$$H_1(k_x, k_y) = \begin{pmatrix} \varepsilon_{E1}(k) & -Ak_+ & Sk_- \\ -Ak & \varepsilon_{H1}(k) & Rk_-^2 \\ Sk_+ & Rk_+^2 & \varepsilon_{E2}(k) \end{pmatrix} \quad (2)$$

$$\varepsilon_{E1}(k) = C + M + B_{E1}(k_x^2 + k_y^2)$$
$$\varepsilon_{H1}(k) = C - M + B_{H1}(k_x^2 + k_y^2)$$
$$\varepsilon_{E2}(k) = C + M + \Delta_{E1E2} + B_{E1}(k_x^2 + k_y^2)$$

Here, C, M, A, B_{E1}, B_{H1}, B_{E2}, Δ_{E1E2}, R, and S are structure parameters, which depend on d_1 and d_2. Parameter Δ_{E1E2} defines the gap between the $E1$ and $E2$ subbands at $\mathbf{k}$ = 0. Because we have kept the inversion symmetry and axial symmetry around the growth direction, $H_{\mathrm{InAs}}(k_x, k_y)$ has a block-diagonal form. The mass parameter M describes inversion between the $E1$ and $H1$ subbands: $M > 0$ corresponds to a trivial BI state, whereas for a QSHI state, $M < 0$. By applying the open boundary condition for $H_{\mathrm{InAs}}(k_x, k_y)$ along the y axis, one can numerically calculate dispersion of helical states, arising at the sample edge at $M < 0$. For instance, the edge state dispersions for the QSHI state at the layer thicknesses marked in Fig. 1C by the open blue symbol are provided in Fig. 2. The structure parameters for $H_{\mathrm{InAs}}(k_x, k_y)$ are given in the Supplementary Materials.

Quantum spin Hall insulator

The essential characteristic of a QSHI is the bandgap values for the bulk states. In the conventional broken-gap QW bilayers, the inverted bandgap opens away from the Γ point of the Brillouin zone because of the interaction between $E1$ and $H1$ subbands at nonzero quasi-momentum. In the case of three-layer InAs/GaSb QWs, the inverted bandgap arises in the Γ point because of quantum confinement, whereas the $E1$-$H1$ interaction vanishes at $\mathbf{k}$ = 0. Because the confinement effect at $\mathbf{k}$ = 0 is much stronger than the $E1$-$H1$ interaction at nonzero $\mathbf{k}$, one can expect that the bandgap in the QSHI state is higher in the three-layer QWs than in InAs/GaSb QW bilayers.

Figure 2A shows the bandgap in the QSHI state as a function of d_1 for d_2 = 14 monolayers (MLs) of GaSb. Here, one ML in the given QW layer corresponds to a half of a lattice constant a_0 in the bulk material. The black and red curves correspond to the structures grown on InAs and GaSb buffers, respectively. It is seen that, starting from $d_1 > d_{1c}$, increasing of d_1 enhances the bandgap, which occurs between the $H1$ and $E1$ levels. When the bandgap approaches to Δ_{E1E2} defined by

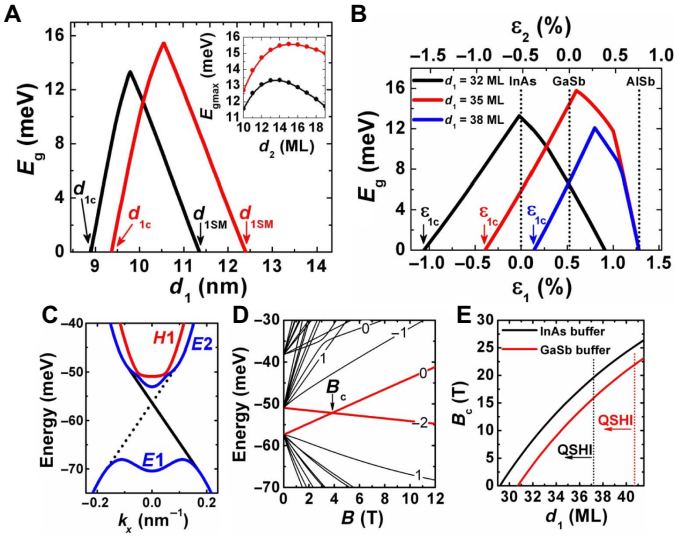

Fig. 2. QSHI in three-layer InAs/GaSb QWs with InAs geometry. (**A**) Bandgap in the QSHI state as a function of d_1 in the InAs/GaSb QWs with InAs geometry at d_2 = 14 MLs, where one ML = 0.5a_0 (a_0 is a lattice constant in the bulk material). The black and red curves correspond to the QWs grown on InAs and GaSb buffers, respectively. The inset shows the maximum gap, which can be achieved at a given value of d_2. (**B**) Bandgap in the QSHI state at different values of d_1 and d_2 = 14 MLs as a function of strain InAs layers ε_1 and GaSb layer ε_2. Three specific cases for the values of ε_1 and ε_2, corresponding to the InAs, GaSb, and AlSb buffers, are marked by vertical dotted lines. (**C**) Band dispersion in the QSHI state calculated on the basis of $H_{InAs}(k_x, k_y)$, with the layer thicknesses marked in Fig. 1C by blue open symbols. Electron- and heavy hole–like subbands are shown in blue and red, respectively. The black curves correspond to the dispersion of the edge states, obtained by numerical diagonalization of $H_{InAs}(k_x, k_y)$ with open boundary conditions along the *y* axis. Different Kramers partners are shown by solid and dotted curves. (**D**) LLs for the QW grown on GaSb buffer at d_1 =32 MLs and d_2 = 14 MLs. The numbers over the curves correspond to the LL indices (*30*). Two red curves are the zero-mode LLs, which are identified within an effective 4 × 4 Hamiltonian for *E*1 and *H*1 subbands (*2*). (**E**) Critical magnetic field B_c as a function of d_1 with d_2 = 14 MLs. The black and red curves correspond to the structures grown on InAs and GaSb buffers, respectively. The dotted vertical lines mark the values of d_{1SM}.

the distance between the *E*1 and *E*2 subbands at **k** = 0, the system transforms into indirect-bandgap QSHI, in which the *H*1 level lies above *E*2 subband (see Fig. 2C). Further increasing of d_1 decreases the indirect bandgap between the *E*1 and *E*2 subbands until it vanishes at $d_1 = d_{1SM}$. The latter causes a transition into SM phase with nonlocal overlapping between conduction and valence subbands. Note that d_{1c} and d_{1SM} depend not only on d_2 but also on the strain in InAs and GaSb layers, which can be varied by changing the buffer material.

Figure 2B provides the bandgap in the QSHI state for the QWs with different values of d_1 and d_2 = 14 MLs as a function of strain in InAs layers ε_1 and GaSb layer ε_2. The values of ε_1 and ε_2 are connected via the lattice constant of the buffer material. It is seen that by tuning the strain, one can successively induce transitions between the BI, QSHI, and SM phases. The value of ε_1, corresponding to the crossing between *E*1 and *H*1 levels, for each of the QWs is marked by vertical arrow and defined as ε_{1c}. It is seen that by using the different values of d_1 and d_2 and by adjusting the strain, one can obtain QSHI with a bandgap of up to 16 meV. The latter is several times greater than the typical bandgap in inverted InAs/GaSb bilayers (*12*). Realization of the given values of ε_1 and ε_2 can be performed by using alloys of various III–V semiconductors (*27*). The vertical dotted lines in Fig. 2B mark the values of ε_1 and ε_2, which correspond to InAs, GaSb, and AlSb buffers. For instance, the QW with d_1 = 35 MLs and d_2 = 14 MLs grown on GaSb buffer (see Fig. 1E) has a QSHI state with a gap close to the maximum value.

It is interesting that the QWs grown on AlSb buffer do not feature a QSHI state. The band inversion defined by the positions of the subband at **k** = 0 is accompanied by nonlocal overlapping between conduction and valence bands. Thus, the variation of InAs and GaSb layer thicknesses drives the system from BI into the SM, avoiding the QSHI state.

Robustness of QSHI in an external magnetic field

A reliable fingerprint of QSHI under applied magnetic field *B* is the characteristic behavior of a particular pair of Landau levels (LLs), the so-called zero-mode LLs (*11*). The origin of this pair of LLs becomes apparent when using an effective 4 × 4 Hamiltonian for *E*1 and *H*1 subbands (*2*). Below a critical field value B_c, the lowest zero-mode LL has an electron-like character and arises from the valence band, whereas the highest zero-mode LL has a heavy hole–like character and splits from the conduction band (see Fig. 2D). In this case, the topological edge states are still present, although they are no longer protected by time-reversal symmetry (*28*, *29*), whereas for larger magnetic fields $B > B_c$, the band ordering becomes normal, and only a trivial state can be found. At the critical magnetic field B_c, corresponding to the crossing of zero-mode LLs, the quantum phase transition between the QSHI and BI states arises.

By neglecting the influence of *E*2 subbands in $H_{InAs}(k_x, k_y)$, we can roughly evaluate the critical magnetic field as (*11*)

$$B_c \approx \frac{\hbar c}{e}\frac{M}{B_{H1} - B_{E1}} \quad (3)$$

where *e* is en elementary charge, $\hbar$ is a Plank constant, and *c* is a velocity of light. For instance, by using the structure parameters for the QW with d_1 = 38 MLs and d_2 = 14 MLs given in the Supplementary Materials, $B_c \sim 10$ T.

Figure 2E provides dependence of B_c on the thickness of InAs layers for the QWs grown on InAs and GaSb buffers calculated by using the eight-band Kane model (*30*). One can see that the critical magnetic field in three-layer InAs/GaSb QWs can reach 20 T, whereas the maximum values of B_c in HgTe/CdTe QWs grown on CdZnTe buffer do not exceed 10 T (*11*).

Three-layer InAs/GaSb QWs with GaSb geometry

Phase diagram

Let us now consider symmetrical GaSb/InAs/GaSb QWs sandwiched between AlSb barriers and grown on (001) GaSb buffer. In contrast to the QWs with InAs geometry, GaSb/InAs/GaSb QWs contain two tunnel-coupled "QWs for holes" with InAs layer as a "middle barrier" (Fig. 3A). We note that the InAs layer of reasonable thicknesses (d_1 > 2 nm) is not transparent for the particles from the hole-like subbands because of large effective mass. Therefore, the hole-like subbands localized in different GaSb layers are decoupled at **k** = 0. However, the mixing between heavy hole– and electron-like states at nonzero **k** leads to the splitting between *H*1 and *H*2 subbands, which can also be contingently considered as odd and even combinations of the hole states in each GaSb layer.

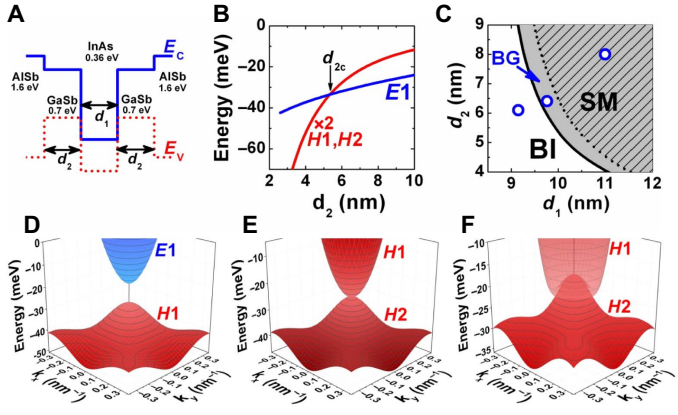

Fig. 3. Band structure of three-layer InAs/GaSb QWs with GaSb geometry. (**A**) Schematic representation of symmetrical three-layer InAs/GaSb QWs with GaSb geometry. The numbers show the bandgap values in materials of the layers. Here, d_1 and d_2 are the thicknesses of InAs and GaSb layers, respectively. The QW is supposed to be grown on (001) GaSb buffer. (**B**) Energy of electron-like (blue curves) and heavy hole–like (red curves) subbands at $\mathbf{k} = 0$, as a function of d_2 at $d_1 = 10$ nm. Zero energy corresponds to the top of valence band in bulk GaSb. (**C**) Phase diagram for different d_1 and d_2. The white open region is a BI phase, whereas the gray-striped region defines an SM phase. The gray open region corresponds to a BG state. (**D** to **F**) 3D plot of the band structure at BI (D), BG (E), and SM (F) phases. The x and y axes are oriented along (100) and (010) crystallographic directions, respectively. The thicknesses of the layers for each phase used in the calculations are marked in (C) by blue open symbols.

Figure 3B shows positions of $E1$, $H1$, and $H2$ subbands at $\mathbf{k} = 0$ and the QW with $d_1 = 10$ nm as a function of d_2. If GaSb layers are thin enough so that $d_2 < d_{2c}$ (where d_{2c} depends on d_1), the $E1$ level lies above the $H1$ and $H2$ subbands, and the QW has a trivial band ordering. For $d_2 > d_{2c}$, the QW has inverted band structure. A phase diagram for the QWs of GaSb geometry is shown in Fig. 3C. The solid curve corresponds to the crossing between $E1$ and $H1$ subbands. It splits the d_1-d_2 plane into the white region of BI phase and the gray region with inverted band structure.

The band inversion in the QWs of GaSb geometry drives the BI into a metal phase with a band structure consisting of two isotropic parabolas, formed by conduction subband $H1$ and valence subband $H2$ touching at $\mathbf{k} = 0$ (see Fig. 3E). This band structure is very similar to the one of natural bilayer graphene (BG) (*26*). The reasons for naming this metal phase as a BG phase will be discussed later. Further increasing of d_1 and d_2 transforms a BG phase into an SM phase, which, in addition to the band touching at $\mathbf{k} = 0$, is also characterized by nonlocal overlapping of the valence subband with the loop of side minima in the conduction subband. This unconventional SM phase is shown by the gray-striped area. The typical band dispersions for BI, BG, and SM phases are provided in the bottom panels.

To derive an effective 2D Hamiltonian for description of quantum phase transition between the BI and BG states in the QWs of GaSb geometry, we directly take into account interaction between $E1$, $H1$, and $H2$ states. In the basis set $|E1,+\rangle$, $|H1,+\rangle$, $|H2,-\rangle$, $|E1,-\rangle$, $|H1,-\rangle$, $|H2,+\rangle$, the effective Hamiltonian is written as

$$H_{\mathrm{GaSb}}(k_x, k_y) = \begin{pmatrix} H_2(k_x, k_y) & 0 \\ 0 & H_2^*(-k_x, -k_y) \end{pmatrix} \quad (4)$$

where

$$H_2(k_x, k_y) = \begin{pmatrix} \varepsilon_{E1}(k) & -Ak_+ & Rk_-^2 \\ -Ak_- & \varepsilon_{H1}(k) & 0 \\ Rk_+^2 & 0 & \varepsilon_{H2}(k) \end{pmatrix} \quad (5)$$

$$\varepsilon_{H2}(k) = C - M + B_{H2}(k_x^2 + k_y^2)$$

Here, the terms $\varepsilon_{E1}(k)$ and $\varepsilon_{H1}(k)$ have the same form as in Eq. 2, and B_{H2} depends only on thicknesses of InAs and GaSb layers. As in Eq. 2, the sign of mass parameter M defines inversion between the $E1$ and $H1$ subbands. The block-diagonal form of $H_{\mathrm{GaSb}}(k_x, k_y)$ results from keeping the inversion and axial symmetry around the growth direction. The structure parameters and comparison with band structure calculations based on the eight-band Kane model are given in the Supplementary Materials as are the structure parameters for $H_{\mathrm{GaSb}}(k_x, k_y)$.

BG phase

As mentioned above, the band inversion in the QWs with GaSb geometry induces a specific metal phase, in which the band structure is very similar to the band structure of natural BG (see Fig. 4A). Here, we show that this BG phase also shares other properties of the BG.

One of the characteristics of natural BG is the unconventional quantum Hall effect (*26*). For natural BG, plateaus in the Hall conductivity σ_{xy} occur at integer multiples of $4e^2/h$, where the level degeneracy $g = 4$ arises from the spin and valley degrees of freedom. Deviation from the conventional case occurs in the vicinity of the charge neutrality point, where there is a step in σ_{xy} of height $8e^2/h$, arising from the eightfold degeneracy of the zero-energy LL. In the BG phase under perpendicular magnetic field, a specific LL with degeneracy two times higher than other LLs also arises. This zero-mode LL, shown in Fig. 4B by the bold red curve (the $h1$ and $h2$ levels), has a pure hole-like character and is formed by the states in the vicinity of the bottom and top of the $H1$ and $H2$ subbands. Because they are touched at $\mathbf{k} = 0$, the zero-mode LL has a doubled degeneracy. The latter can be analytically shown by using an effective 2D Hamiltonian $H_{\mathrm{GaSb}}(k_x, k_y)$. The doubled degeneracy of the zero-mode LL requires two times more carriers to fill it, so the transition between the corresponding plateaus should be twice as wide in density as others, and the σ_{xy} step between the plateaus are expected to be $2e^2/h$ instead of e^2/h.

In natural BG, a bandgap can be opened by breaking the inversion symmetry, for instance, by electric field applied perpendicularly to the sample plane. The QWs with GaSb geometry also holds this property. Figure 4C shows the band dispersion in a perpendicular electric field of 5 kV/cm. Even in this case, the dispersion curves are very similar to the band structure of natural BG in an external electric field (*31*). However, the strong spin-orbit interaction in the QWs with GaSb geometry removes the spin degeneracy at nonzero quasi-momentum due to the Rashba effect (*32*). Figure 4D shows the bandgap Δ values in the BG phase as a function of applied electric field. The bandgap is electrically tunable because it is in natural BG, although its dependence on an electric field in the InAs/GaSb QWs has nonmonotonic behavior. Note that an inversion asymmetry in the QWs with GaSb geometry also splits the zero-mode LLs, removing this doubled degeneracy order. Therefore, we anticipate the recovery of the equidistant sequence of plateaus in the Hall conductivity discussed above, such as for gate-biased natural BG (*33*).

Previously, the BG phase was predicted for two tunnel-coupled HgTe QWs (*25*). Here, we show the existence of this phase in the

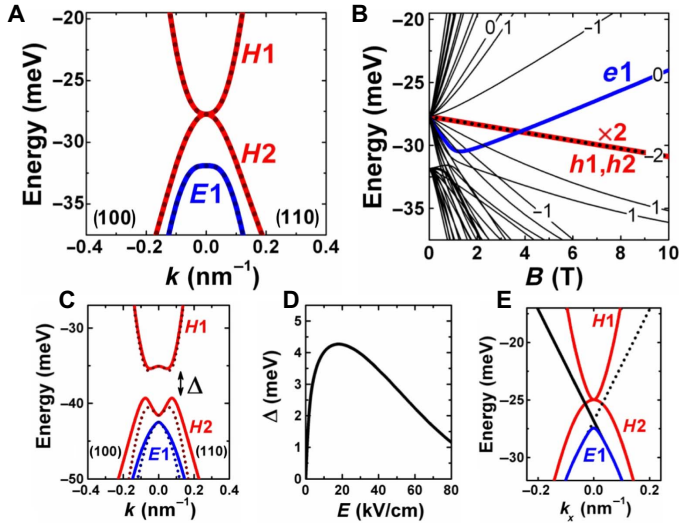

Fig. 4. BG phase in three-layer InAs/GaSb QWs with GaSb geometry. (**A**) Band dispersions for a BG phase in the QW grown on GaSb buffer at d_1 = 10 nm and d_2 = 6 nm. Electron- and hole-like subbands are shown in blue and red, respectively. Solid and dotted curves correspond to different spin states. (**B**) LL fan chart. The zero-mode LL, which has doubled degeneracy order as compared with other levels, is marked by red bold curve (the *h*1 and *h*2 levels). This LL is formed by states of both *H*1 and *H*2 subbands. LL, containing only the states from the *E*1 subband in high magnetic fields, is given in blue. The crossing between the *e*1 and *h*1 LLs, arising at critical magnetic field $B_c \approx 3.7$ T, leads to the phase transition into normal (noninverted) band structure, as it is in single HgTe QW (*11*). (**C**) Band dispersions in an electric field of 5 kV/cm oriented perpendicular the QW plane. (**D**) Bandgap as a function of an applied electric field. (**E**) Band dispersion for a BG phase, calculated on the basis of $H_{GaSb}(k_x, k_y)$ with the layer thicknesses marked in Fig. 3C by blue open symbol. The black curves correspond to the dispersion of the edge states, obtained by numerical diagonalization of $H_{GaSb}(k_x, k_y)$ with open boundary conditions along the *y* axis. Different Kramers partners are shown by solid and dotted curves.

three-layer InAs/GaSb QWs. As well as in double HgTe QWs, there is also an additional specific LL, which is only formed at high magnetic fields by the states from *E*1 subband. In weak magnetic fields, this LL, denoted as *e*1 in Fig. 4D, is mixed with the states from the *H*1 subband. The latter results in anticrossing between *e*1 LL and LLs from the *H*1 subband in magnetic fields below 2 T. The crossing between the *e*1 and zero-mode LL, arising at critical magnetic field $B_c \sim 3.7$ T, corresponds to the transition from inverted to trivial band ordering (*11*).

The main difference between natural BG and the BG phase is that the electrons in the QWs with GaSb geometry are not chiral particles, although they mimic some characteristics of natural BG. In addition, in the BG phase, the gapless bulk states and spin-polarized edge channels coexist. The latter can be shown by solving the eigenvalue problem for $H_{GaSb}(k_x, k_y)$ at $M < 0$ with the open boundary condition along one of the directions. A typical picture of the edge states in the BG phase, established within the effective 2D model for the layer thicknesses marked in Fig. 3C by blue open symbol, is provided in Fig. 4E.

Massless Dirac fermions in three-layer InAs/GaSb QWs

As discussed above, inversion symmetry in the growth direction of the three-layer InAs/GaSb QWs leads to the crossing of the *E*1 and *H*1 subbands in the Γ point of the Brillouin zone. Let us show that this crossing yields massless Dirac fermions in a 2D system. In the vicinity of crossing of *E*1 and *H*1 subbands, the terms quadratic in quasi-momentum in both effective Hamiltonians can be neglected.

For the QWs with InAs geometry, the latter corresponds to the limit of large Δ_{E1E2}. Therefore, $H_1(k_x, k_y)$ can be projected on the subspace, containing the *E*1 and *H*1 states. Because we are not interested in terms quadratic in **k**, the projection is performed by simply eliminating the third row and column of the matrix in Eq. 2 and by setting B_{E1} and B_{H1} to zero. In the case of the QWs with GaSb geometry, keeping linear in **k** terms in $H_2(k_x, k_y)$ results to decoupling of the *H*2 subband from the *E*1 and *H*1 states. Therefore, the block describing the *E*1 and *H*1 subbands can be considered separately.

Without loss of generality, we can set $C = 0$ and the 2D Hamiltonian for the states in the vicinity of $\mathbf{k} = 0$ in the crossed *E*1 and *H*1 subbands ($M = 0$), for both types of the QWs takes the form

$$H_{1,2}^{(E1+,H1+)}(k_x, k_y) \cong \begin{pmatrix} 0 & \hbar v_F k_+ \\ \hbar v_F k_- & 0 \end{pmatrix} \quad (6)$$

The similar Hamiltonian can be also derived for $H_1^*(-k_x, -k_y)$ and $H_2^*(-k_x, -k_y)$. It is seen that Eq. 6 corresponds to a massless Dirac Hamiltonian with Fermi velocity v_F, defined by parameter *A* in Eqs. 2 and 5.

Figure 5 shows the band dispersion for the QWs of both geometries, when the *E*1 and *H*1 subbands are crossed. The layer thicknesses correspond to the crossing of the *E*1 and *H*1 subbands shown in Figs. 1B and 2B. Because the hybridization between *E*1 and *H*1 subbands vanishes at $\mathbf{k} = 0$, it results in the gapless state with 2D massless Dirac fermions, just like in HgTe/CdTe QWs with critical thicknesses (*15*). The linear band dispersion at small **k** is seen. However, in the QWs with GaSb geometry, the Dirac cone is accompanied by an additional decoupled "massive" branch of *H*2 subband arising at the crossing point that is similar to the case of two tunnel-coupled HgTe QWs (*25*).

The bottom panels in Fig. 5 provide v_F for massless Dirac fermions as a function of d_2 in the QWs with InAs and GaSb geometries. It is seen that Fermi velocity is varied from 1×10^5 to 3×10^5 m/s, depending on the GaSb layer thicknesses. These values are several times lower than the ones in graphene (~10^6 m/s) and HgTe/CdTe QWs (*15*).

Finally, we stress the effect of strain on v_F of the massless particle, arising because of lattice-mismatch constant in the QW layers and buffers. It is seen that increasing tensile strain of InAs layers ($\varepsilon_1 > 0$) in the QWs with both geometries enhances v_F. As we have discussed previously, at high values of ε_1, the band inversion drives the QWs with InAs geometry from BI into SM phase, avoiding the QSHI state. In this case, the Dirac cone in the Γ point of the Brillouin zone arising at critical layer thicknesses is accompanied by the side maxima of the valence band overlapping with the conduction band bottom. We note that, in the QWs with GaSb geometry, the band inversion does not occur at high values of ε_1. For instance, the QWs grown on AlSb buffer have trivial band ordering at all layer thicknesses.

Large-gap QSHI in three-layer QWs with InAs geometry

We have demonstrated that the three-layer QWs with InAs geometry and HgTe/CdTe QWs share the same possible phases and feature the comparable bandgaps in the QSHI state. As has been demonstrated recently (*16*), compressive strain in HgTe QWs extends the bandgap of QSHI up to 60 meV at reasonable values of the strain. Now, we address the question of whether the bandgap of the QSHI state in three-layer InAs/GaSb the QWs can be enhanced up to the same values of compressively strained HgTe QWs. However, if either compressive or tensile

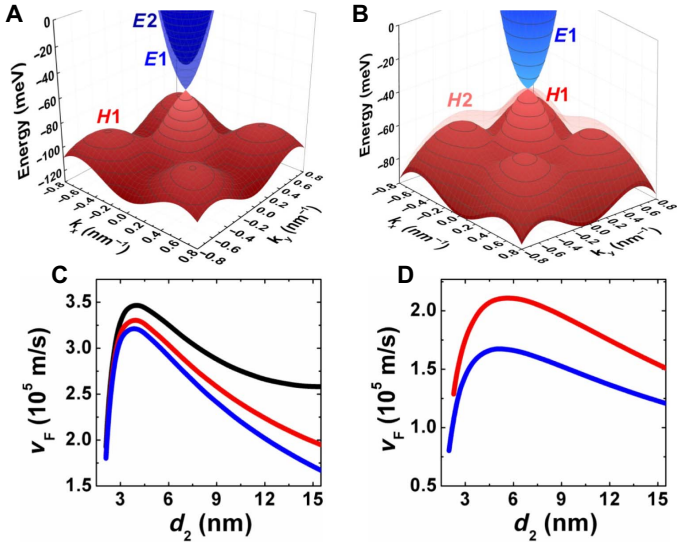

Fig. 5. Massless Dirac fermions in three-layer InAs/GaSb QWs. (**A** and **B**) 3D plot of the band dispersions of three-layer InAs/GaSb QWs of InAs geometry (A) and GaSb geometry (B) both grown on GaSb buffer. The values of d_1 and d_2 correspond to the crossing of *E*1 and *H*1 subbands, shown in Figs. 1B and 2B. (**C** and **D**) Fermi velocity v_F of massless Dirac fermions as a function of GaSb layer thickness for the QWs of InAs geometry (C) and GaSb geometry (D) grown on different buffers: black curves, AlSb; red curves, GaSb; blue curves, InAs.

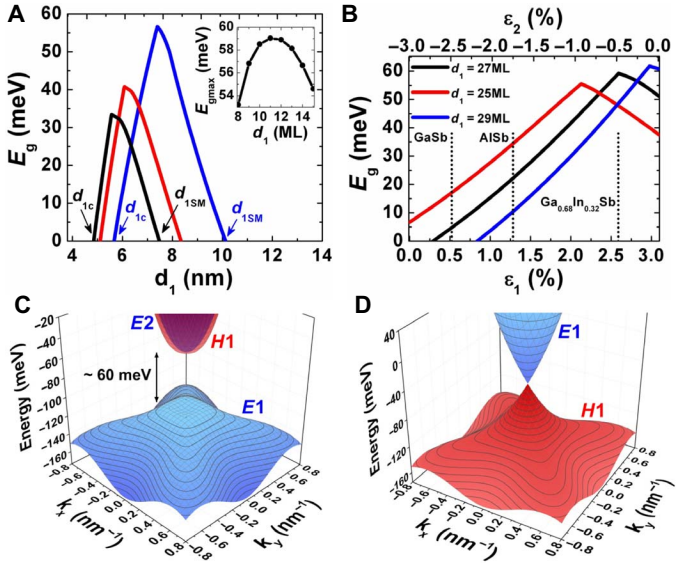

Fig. 6. Large-gap QSHI in three-layer QWs with InAs geometry. (**A**) Bandgap in the QSHI state for three-layer InAs/$Ga_{0.6}In_{0.4}Sb$ QWs of InAs geometry as a function of d_1 at d_2 = 14 MLs (where one ML equals to a half of lattice constant in the bulk material). The black, red, and blue curves correspond to the structures grown on GaSb, AlSb, and $Ga_{0.68}In_{0.32}Sb$ buffers, respectively. The inset shows the maximum gap, which can be achieved at a given value of d_2, in the QW grown on $Ga_{0.68}In_{0.32}Sb$ buffer. (**B**) Bandgap in the QSHI state for the InAs/$Ga_{0.6}In_{0.4}Sb$ QWs with different values of d_1 and d_2 = 11 MLs as a function of strain in InAs layers ε_1 and $Ga_{0.6}In_{0.4}Sb$ layer ε_2. Three specific cases for the values of ε_1 and ε_2, corresponding to the GaSb, AlSb, and $Ga_{0.68}In_{0.32}Sb$ buffers, are marked by vertical dotted lines. (**C** and **D**) 3D plot of the band dispersion for the InAs/$Ga_{0.6}In_{0.4}Sb$ QW grown on $Ga_{0.68}In_{0.32}Sb$ buffer at d_2 = 11 MLs, d_1 = 27 MLs (C) and $d_1 = d_{1c}$ ($d_{1c} \approx 6$ nm) (D). The *x* and *y* axes are oriented along (100) and (010) crystallographic directions, respectively.

strain is large enough, it destroys the QSHI state in three-layer InAs/GaSb QWs and induces a phase transition into the BI or SM phase, respectively (see Fig. 2B).

To increase the inverted bandgap in the InAs-designed QWs, we therefore replace the middle GaSb layer in the QW by a $Ga_{1-x}In_xSb$ alloy. Previously, Smith and Mailhiot (*34*) have found that this replacement significantly enhances the inverted bandgap in strained InAs/GaInSb superlattice (SL). Recently, this idea has been applied to the InAs/GaInSb QW bilayers (*21*), in which the bandgap can be increased up to 20 meV.

Figure 6A shows the bandgap in the QSHI state in three-layer InAs/$Ga_{0.6}In_{0.4}Sb$ QW with InAs geometry as a function of d_1 at d_2 = 14 MLs. The black, red, and blue curves correspond to the structures grown on GaSb, AlSb, and $Ga_{0.68}In_{0.32}Sb$ buffer, respectively. It is seen that the inverted bandgap in the strained InAs/$Ga_{0.6}In_{0.4}Sb$ QW is several times larger than the values obtained for the three-layer InAs/GaSb QWs. The inset shows the maximum gap in the strained QW grown on $Ga_{0.68}In_{0.32}Sb$ buffer, which can be achieved at given value of d_2.

Figure 6B provides the QSHI bandgap in the InAs/$Ga_{0.6}In_{0.4}Sb$ QWs with different values of d_1 and d_2 = 11 MLs as a function of strain InAs layers ε_1 and $Ga_{0.6}In_{0.4}Sb$ layer ε_2. Note that the values of ε_1 and ε_2 are connected via the lattice constant of the buffer material. Figure 6B proves theoretically that, by adjusting the strain for different values of d_1 and d_2, one can obtain a QSHI with a large bandgap. It is seen that the InAs/$Ga_{0.6}In_{0.4}Sb$ QW with d_1 = 27 MLs and d_2 = 11 MLs grown on $Ga_{0.68}In_{0.32}Sb$ buffer features a bandgap in the QSHI state of about 60 meV. The band structure for this QW is shown in Fig. 6C. We have considered the case of symmetrical InAs/GaInSb/InAs QWs. We note that the bandgap in these QWs can be tuned by varying the strength of an applied electric field or by growing the InAs layers of different thicknesses. However, the maximum QSHI bandgap in the three-layer InAs/$Ga_{0.6}In_{0.4}Sb$ QWs can be achieved only in symmetrical geometry (see the Supplementary Materials).

In addition to large-gap QSHI, the InAs/$Ga_{0.6}In_{0.4}Sb$ QWs at critical thicknesses feature massless Dirac fermions with Fermi velocity (up to 7×10^5 m/s) higher than in the InAs/GaSb/InAs QWs. Moreover, a linearity of their energy dispersion persists in much higher energy ranges. The latter can be seen by comparing Figs. 6D and 5A.

DISCUSSION

To summarize, we have considered realization of phases in multilayer InAs/Ga(In)Sb QWs containing broken-gap band alignment at the two interfaces. We note that our results are general and valid for any type II QW heterostructures. So far, multilayer type II heterostructures based on InAs, GaSb, InSb, AlSb, and their alloys have been interesting in view of laser and detector applications in mid-infrared (IR) and terahertz range. We believe that theoretical predictions performed here make the multilayer type II QWs attractive for realistic pseudorelativistic electronics and high-temperature QSHI devices.

In particular, MBE growth technology for InAs/GaInSb heterostructures is well developed nowadays. Since the 2000s, it has been widely used for the growth of strained InAs/$Ga_{1-x}In_xSb$ SL for mid-IR photodetectors with $x < 0.4$. Significant progress in the MBE technology of InAs/GaInSb, which has been achieved very recently (*35*, *36*), allows pseudomorphic growth of 40-period strained InAs/$Ga_{0.6}In_{0.4}Sb$ SL with good structural and surface quality. Because the InAs/$Ga_{1-x}In_xSb$

QW can be contingently considered as a "single-period SL," it should not require a large critical layer thickness for the pseudomorphic growth. Therefore, the pseudomorphic growth of the InAs/$Ga_{1-x}In_xSb$ QW structures may be possible even with $x > 0.4$. An inverted bandgap of more than 60 meV is expected in these QWs.

Another way to increase a bandgap in QSHI state is based on utilization of InAsSb alloys. Having the lowest bandgap among all III–V semiconductors, InAsSb alloys attract attention both for fundamental research as a potential alternative to HgCdTe for long-wavelength IR optoelectronics. The recent development of the MBE technique made it possible to grow high-quality InAsSb bulk films (*37*) and type II strained $InAs_{1-x}Sb_x/InAs_{1-y}Sb_y$ SL (*38*). Preliminary estimations of band structure calculations performed for a modeled three-layer InAsSb/GaInSb and $InAs_{1-x}Sb_x/InAs_{1-y}Sb_y$ QWs also show theoretical possibility for the large gap in the QSHI state of more than 60 meV but at lower strain in the QW layers.

Finally, we stress an important advantage of QSHI based on the three-layer InAs/GaInSb QWs as compared with the one based on HgTe/CdTe QWs. Because temperature does not affect the ordering of the Γ_6 and Γ_8 bands in bulk InSb, InAs, GaSb, and AlSb semiconductors, one can expect a substantially weaker dependence of the bandgap on temperature in the multilayer broken-gap QWs than in HgTe/CdHgTe QWs.

Very recently, the quantum spin Hall effect in 1T′-WTe_2 MLs at temperatures up 100 K has been reported (*39*). We note that this is the highest temperature at which the main hallmark of the QSHI state has ever been observed. This high temperature is consistent with a relatively large inverted bandgap (~45 meV) in the 1T′-WTe_2 extracted from recent spectroscopy (*40*, *41*). Moreover, it is suspected that the 100-K temperature may not be an intrinsic limit of 1T′-WTe_2 MLs. Improvements in device quality may enable observation of the QSHI at even higher temperatures and for longer edge channels. In view of these novel experimental results and mature fabrication technology, the multilayer broken-gap QWs based on III–V semiconductors become extremely attractive for high-temperature topological electronics.

MATERIALS AND METHODS

Band structure calculations were performed by using the eight-band Kane model (*30*), which directly takes into account the interactions between Γ_6, Γ_8, and Γ_7 bands in bulk materials. This model well describes the electronic states in a wide range of narrow-gap semiconductor QWs, particularly in the broken-gap InAs/GaSb QWs (*12*). In the eight-band Kane Hamiltonian, we also took into account the terms, describing the strain effect arising because of the mismatch of lattice constants in the buffer, QW layers, and AlSb barriers. To calculate LLs, we used the so-called axial approximation. Within this approximation, one keeps in-plane rotation symmetry by omitting the warping terms in the Hamiltonian. The calculations had been performed by expanding the eight-component envelope wave functions in the basis set of plane waves and by numerical solution of the eigenvalue problem. Details of calculations, notations of the LLs, and the form of the Hamiltonian can be found in the study of Krishtopenko *et al.* (*30*). Parameters for the bulk materials and valence band offsets used in the eight-band Kane model are taken from Vurgaftman *et al.* (*27*). Here, we considered the structures grown along (001) crystallographic orientation.

To derive effective six-band 2D Hamiltonians $H_{InAs}(k_x, k_y)$ and $H_{GaSb}(k_x, k_y)$, valid in the vicinity of the Γ point from the eight-band Kane model, we followed the procedure proposed by Bernevig *et al.* (*2*) and described in detail in the supplementary materials of Krishtopenko *et al.* (*25*). First, we split the Kane Hamiltonian $\mathbf{H}^{Kane}$ into two parts, $\mathbf{H}^{Kane} = \mathbf{H}^{(0)}(k_z) + \mathbf{H}^{(1)}(k_z, k_x, k_y)$, where $\mathbf{H}^{(0)}(k_z)$ is the Kane Hamiltonian at $k_x = k_y = 0$. In our case, the z axis is oriented along (001) direction, whereas the x and y axes correspond to the (100) and (010) directions, respectively. Then, we numerically diagonalized $\mathbf{H}^{(0)}(k_z)$ to obtain the energies and envelope functions and to classify electronic levels as electron-like *En*, heavy hole–like *Hn*, light hole–like *LHn*, or spin-off–like *SOn* levels ($n = 1, 2, \ldots$), as it is performed by König *et al.* (*11*).

Then, we grouped the eigenstates of $\mathbf{H}^{(0)}(k_z)$ into *A* and *B* subsets. The *A* subset includes the basis sets of $\{|E1,\pm\rangle, |H1,\pm\rangle, |E2,\pm\rangle\}$ levels for the InAs-designed QWs and $\{|E1,\pm\rangle, |H1,\pm\rangle, |H2,\pm\rangle\}$ for the GaSb-designed structures. In the *B* subset, we considered eight above-lying, electron-like states and eight subbands for light hole– and heavy hole–like states. All the other subbands were neglected because they were well separated in energy. The states in both classes were not coupled because they are eigenstates of $\mathbf{H}^{(0)}(k_z)$. The presence of $\mathbf{H}^{(1)}(k_z, k_x, k_y)$ introduces the mixing between the states from two subsets. To derive effective 2D Hamiltonians $H_{InAs}(k_x, k_y)$ and $H_{GaSb}(k_x, k_y)$, we treated $\mathbf{H}^{(1)}(k_z, k_x, k_y)$ as a small perturbation and applied the second-order Löwdin perturbation method to eliminate the coupling between the states from different subsets

$$H_{\text{eff}}(k_x, k_y)_{m,m'} = E_m\delta_{m,m'} + H^{(1)}_{m,m'} + \frac{1}{2}\sum_l H^{(1)}_{m,l}H^{(1)}_{l,m'}\left(\frac{1}{E_m - E_l} + \frac{1}{E_{m'} - E_l}\right)$$

Here, the indices m, m' correspond to states in set *A*, the indices l correspond to the states in set *B*, and $H^{(1)}_{m,m'}$ is the matrix element of $\mathbf{H}^{(1)}(k_z, k_x, k_y)$, calculated by using the envelope function of $\mathbf{H}^{(0)}(k_z)$. Parameters for both effective Hamiltonians for different thicknesses of InAs d_1 and d_2 GaSb layers are provided in the Supplementary Materials.

To calculate dispersion of the edge states on a single edge, we dealt with a system on a half-plane of $y \le 0$ and replaced k_y by $-i\partial_y$ in $H_{InAs}(k_x, k_y)$ and $H_{GaSb}(k_x, k_y)$. If $M < 0$, both types of three-layer InAs/GaSb QWs support the edge states, which exponentially decay at $y \to -\infty$. The 2D effective Hamiltonians $H_{InAs}(k_x, -i\partial_y)$ and $H_{GaSb}(k_x, -i\partial_y)$ are block-diagonal, and the eigenvalue problem of the upper and lower blocks was solved separately. To find the energy spectrum of the edge states for each block, we numerically solved the Schrödinger equation with the boundary condition for the wave function to vanish at $y = 0$. Taking into account the translation invariance along the x axis, the wave function of the edge states has the form

$$\Psi_{\text{edge}}(x, y)\frac{e^{ik_x x}}{\sqrt{L_x}}\sum_{n=1}^{3}\alpha_n e^{\lambda_n y}C_n^{(\text{edge})}$$

where k_x is the wave vector along the edge, L_x is the sample size along the x axis, α_n is the coefficient determined by the boundary conditions, λ_n is the complex-valued reciprocal lengths, and $C_n^{(\text{edge})}$ is the position-independent normalized three-component columns.

For a given wave vector k_x, relation $\lambda_n(E_{\text{edge}})$ and columns $C_n^{(\text{edge})}$ are found from the matrix equation

$$H_{1,2}(k_x, -i\lambda)C^{(\text{edge})} = E_{\text{edge}}C^{(\text{edge})}$$

Note that λ_n, in general, can be complex, corresponding to a mixture of the edge and bulk states. The energy spectrum of the edge states is found from the condition of wave function decay at $y \to -\infty$ [by implying real part of complex number Re (a real part of complex number) $\lambda_n > 0$] and from the boundary condition at $y \to 0$

$$\sum_{n=1}^{4} \alpha_n C_n^{(\text{edge})} = 0$$

The energy spectrum of the edge states for the lower blocks in $H_{\text{InAs}}(k_x, k_y)$ and $H_{\text{GaSb}}(k_x, k_y)$ is found in a similar manner.

SUPPLEMENTARY MATERIALS

Supplementary material for this article is available at http://advances.sciencemag.org/cgi/content/full/4/4/eaap7529/DC1

Supplementary Text

fig. S1. Comparison between calculations within the eight-band Kane model and by using the effective Hamiltonians for three-layer InAs/GaSb QWs.

fig. S2. Bandgap in QSHI state in asymmetrical three-layer InAs/GaInSb QWs.

table S1. Parameters involved in the effective Hamiltonian $H_{\text{InAs}}(k_x, k_y)$ for three-layer InAs/GaSb QWs with InAs geometry grown on GaSb buffer.

table S2. Parameters of the effective 2D Hamiltonian $H_{\text{GaSb}}(k_x, k_y)$ for three-layer InAs/GaSb QWs with GaSb geometry grown on GaSb buffer.

REFERENCES AND NOTES

1. M. Z. Hasan, C. L. Kane, Colloquium: Topological insulators. *Rev. Mod. Phys.* **82**, 3045 (2010).
2. B. A. Bernevig, T. L. Hughes, S.-C. Zhang, Quantum spin Hall effect and topological phase transition in HgTe quantum wells. *Science* **314**, 1757–1761 (2006).
3. L. Fu, C. L. Kane, Superconducting proximity effect and Majorana fermions at the surface of a topological insulator. *Phys. Rev. Lett.* **100**, 096407 (2008).
4. J. Nilsson, A. R. Akhmerov, C. W. J. Beenakker, Splitting of a cooper pair by a pair of Majorana bound states. *Phys. Rev. Lett.* **101**, 120403 (2008).
5. C.-C. Liu, W. Feng, Y. Yao, Quantum spin Hall effect in silicene and two-dimensional germanium. *Phys. Rev. Lett.* **107**, 076802 (2011).
6. Z. Liu, C. X. Liu, Y. S. Wu, W. H. Duan, F. Liu, J. Wu, Stable nontrivial Z_2 topology in ultrathin Bi (111) films: A first-principles study. *Phys. Rev. Lett.* **107**, 136805 (2011).
7. X. Qian, J. Liu, L. Fu, J. Li, Quantum spin Hall effect in two-dimensional transition metal dichalcogenides. *Science* **346**, 1344–1347 (2014).
8. A. Bansil, H. Lin, T. Das, Colloquium: Topological band theory. *Rev. Mod. Phys.* **88**, 021004 (2016).
9. F. Reis, G. Li, L. Dudy, M. Bauernfeind, S. Glass, W. Hanke, R. Thomale, J. Schäfer, R. Claessen, Bismuthene on a SiC substrate: A candidate for a high-temperature quantum spin Hall material. *Science* **357**, 287–290 (2017).
10. C. L. Kane, E. J. Mele, Z_2 topological order and the quantum spin Hall effect. *Phys. Rev. Lett.* **95**, 146802 (2005).
11. M. König, S. Wiedmann, C. Brüne, A. Roth, H. Buhmann, L. W. Molenkamp, X.-L. Qi, S.-C. Zhang, Quantum spin Hall insulator state in HgTe quantum wells. *Science* **318**, 766–770 (2007).
12. C. Liu, T. L. Hughes, X.-L. Qi, K. Wang, S.-C. Zhang, Quantum spin Hall effect in inverted type-II semiconductors. *Phys. Rev. Lett.* **100**, 236601 (2008).
13. I. Knez, R.-R. Du, G. Sullivan, Evidence for helical edge modes in inverted InAs/GaSb quantum wells. *Phys. Rev. Lett.* **107**, 136603 (2011).
14. L. G. Gerchikov, A. V. Subashiev, Interface states in subband structure of semiconductor quantum wells. *Phys. Status Solidi B* **160**, 443–457 (1990).
15. B. Büttner, C. X. Liu, G. Tkachov, E. G. Novik, C. Brüne, H. Buhmann, E. M. Hankiewicz, P. Recher, B. Trauzettel, S. C. Zhang, L. W. Molenkamp, Single valley Dirac fermions in zero-gap HgTe quantum wells. *Nat. Phys.* **7**, 418–422 (2011).
16. P. Leubner, L. Lunczer, C. Brüne, H. Buhmann, L. W. Molenkamp, Strain engineering of the band gap of HgTe quantum wells using superlattice virtual substrates. *Phys. Rev. Lett.* **117**, 086403 (2016).
17. S. Wiedmann, A. Jost, C. Thienel, C. Brüne, P. Leubner, H. Buhmann, L. W. Molenkamp, J. C. Maan, U. Zeitler, Temperature-driven transition from a semiconductor to a topological insulator. *Phys. Rev. B* **91**, 205311 (2015).
18. M. Marcinkiewicz, S. Ruffenach, S. S. Krishtopenko, A. M. Kadykov, C. Consejo, D. B. But, W. Desrat, W. Knap, J. Torres, A. V. Ikonnikov, K. E. Spirin, S. V. Morozov, V. I. Gavrilenko, N. N. Mikhailov, S. A. Dvoretskii, F. Teppe, Temperature-driven single-valley Dirac fermions in HgTe quantum wells. *Phys. Rev. B* **96**, 035405 (2017).
19. F. Teppe, M. Marcinkiewicz, S. S. Krishtopenko, S. Ruffenach, C. Consejo, A. M. Kadykov, W. Desrat, D. But, W. Knap, J. Ludwig, S. Moon, D. Smirnov, M. Orlita, Z. Jiang, S. V. Morozov, V. I. Gavrilenko, N. N. Mikhailov, S. A. Dvoretskii, Temperature-driven massless Kane fermions in HgCdTe crystals. *Nat. Commun.* **7**, 12576 (2016).
20. S. Murakami, S. Iso, Y. Avishai, M. Onoda, N. Nagaosa, Tuning phase transition between quantum spin Hall and ordinary insulating phases. *Phys. Rev. B* **76**, 205304 (2007).
21. L. Du, W. Lou, X. Wu, X. Liu, Z. Han, C. Zhang, G. Sullivan, A. Ikhlassi, K. Chang, R. R. Du, Tuning edge states in strained-layer InAs/GaInSb quantum spin Hall insulators. *Phys. Rev. Lett.* **119**, 056803 (2017).
22. I. Knez, R.-R. Du, G. Sullivan, Andreev reflection of helical edge modes in InAs/GaSb quantum spin Hall insulator. *Phys. Rev. Lett.* **109**, 186603 (2012).
23. V. S. Pribiag, A. J. Beukman, F. Qu, M. C. Cassidy, C. Charpentier, W. Wegscheider, L. P. Kouwenhoven, Edge-mode superconductivity in a two-dimensional topological insulator. *Nat. Nanotechnol.* **10**, 593–597 (2015).
24. F. Qu, A. J. Beukman, S. Nadj-Perge, M. Wimmer, B. M. Nguyen, W. Yi, J. Thorp, M. Sokolich, A. A. Kiselev, M. J. Manfra, C. M. Marcus, L. P. Kouwenhoven, Electric and magnetic tuning between the trivial and topological phases in InAs/GaSb double quantum wells. *Phys. Rev. Lett.* **115**, 036803 (2015).
25. S. S. Krishtopenko, W. Knap, F. Teppe, Phase transitions in two tunnel-coupled HgTe quantum wells: Bilayer graphene analogy and beyond. *Sci. Rep.* **6**, 30755 (2016).
26. K. S. Novoselov, E. McCann, S. V. Morozov, V. I. Fal'ko, M. I. Katsnelson, U. Zeitler, D. Jiang, F. Schedin, A. K. Geim, Unconventional quantum Hall effect and Berry's phase of 2π in bilayer graphene. *Nat. Phys.* **2**, 177–180 (2006).
27. I. Vurgaftman, J. R. Meyer, L. R. Ram-Mohan, Band parameters for III-V compound semiconductors and their alloys. *J. Appl. Phys.* **89**, 5815–5875 (2001).
28. G. Tkachov, E. M. Hankiewicz, Ballistic quantum spin Hall state and enhanced edge backscattering in strong magnetic fields. *Phys. Rev. Lett.* **104**, 166803 (2010).
29. S.-B. Zhang, Y.-Y. Zhang, S.-Q. Shen, Robustness of quantum spin Hall effect in an external magnetic field. *Phys. Rev. B* **90**, 115305 (2014).
30. S. S. Krishtopenko, I. Yahniuk, D. B. But, V. I. Gavrilenko, W. Knap, F. Teppe, Pressure- and temperature-driven phase transitions in HgTe quantum wells. *Phys. Rev. B* **94**, 245402 (2016).
31. T. Ohta, A. Bostwick, T. Seyller, K. Horn, E. Rotenberg, Controlling the electronic structure of bilayer graphene. *Science* **313**, 951–954 (2006).
32. E. I. Rashba, Properties of semiconductors with an extremum loop. 1. Cyclotron and combinational resonance in a magnetic field perpendicular to the plane of the loop. *Sov. Phys. Solid. State* **2**, 1109–1122 (1960).
33. E. V. Castro, K. S. Novoselov, S. V. Morozov, N. M. R. Peres, J. M. B. Lopes dos Santos, J. Nilsson, F. Guinea, A. K. Geim, A. H. Castro Neto, Biased bilayer graphene: Semiconductor with a gap tunable by the electric field effect. *Phys. Rev. Lett.* **99**, 216802 (2007).
34. D. L. Smith, C. Mailhiot, Proposal for strained type II superlattice infrared detectors. *J. Appl. Phys.* **62**, 2545 (1987).
35. M. Patrashin, I. Hosako, K. Akahane, Type-II InAs/GaInSb superlattices for terahertz range photodetectors. *Proc. SPIE* **8188**, 81880G (2011).
36. M. Patrashin, K. Akahane, N. Sekine, I. Hosako, Molecular beam epitaxy of strained-layer InAs/GaInSb superlattices for long-wavelength photodetectors. *J. Cryst. Growth* **477**, 86–90 (2017).
37. S. Suchalkin, J. Ludwig, G. Belenky, B. Laikhtman, G. Kipshidze, Y. Lin, L. Shterengas, D. Smirnov, S. Luryi, W. L. Sarney, S. P. Svensson, Electronic properties of unstrained unrelaxed narrow gap $InAs_xSb_{1-x}$ alloys. *J. Phys. D Appl. Phys.* **49**, 105101 (2016).
38. S. Suchalkin, G. Belenky, M. Ermolaev, S. Moon, Y. Jiang, D. Graf, D. Smirnov, B. Laikhtman, L. Shterengas, G. Kipshidze, S. P. Svensson, W. L. Sarney, Engineering Dirac materials: Metamorphic $InAs_{1-x}Sb_x/InAs_{1-y}Sb_y$ superlattices with ultralow bandgap. *Nano Lett.* **18**, 412–417 (2018).
39. S. Wu, V. Fatemi, Q. D. Gibson, K. Watanabe, T. Taniguchi, R. J. Cava, P. Jarillo-Herrero, Observation of the quantum spin Hall effect up to 100 kelvin in a monolayer crystal. *Science* **359**, 76–79 (2018).
40. Z. Fei, T. Palomaki, S. Wu, W. Zhao, X. Cai, B. Sun, P. Nguyen, J. Finney, X. Xu, D. H. Cobden, Edge conduction in monolayer WTe_2. *Nat. Phys.* **13**, 677–682 (2017).
41. S. Tang, C. Zhang, D. Wong, Z. Pedramrazi, H.-Z. Tsai, C. Jia, B. Moritz, M. Claassen, H. Ryu, S. Kahn, J. Jiang, H. Yan, M. Hashimoto, D. Lu, R. G. Moore, C. Hwang, C. Hwang, Z. Hussain, Y. Chen, M. M. Ugeda, Z. Liu, X. Xie, T. P. Devereaux, M. F. Crommie, S.-K. Mo, Z.-X. Shen, Quantum spin Hall state in monolayer 1T′-WTe_2. *Nat. Phys.* **13**, 683 (2017).

Acknowledgments: We are grateful to E. Tournié [Institute of Electronics and Systems (IES), Montpellier], J. Torres (IES, Montpellier), and D. Carpentier (École Normale Supérieure de Lyon) for helpful discussions on the manuscript. **Funding:** This work was supported by the Occitanie region via the "Gepeto Terahertz platform" by the Era.Net-Rus Plus

"Terasens" project by the CNRS through the emergence project 2016, by Montpellier University through the "Terahertz Occitanie Platform," and by the Russian Ministry of Education and Science (MK-1136.2017.2). Investigation of multilayer InAs/GaInSb QWs was supported by project no. 17-72-10158 from the Russian Science Foundation. **Author contributions:** All authors contributed to the main contents of this work. S.S.K. conceived and supervised the project and also did analytical and numerical calculations. The figures were prepared by S.S.K. The paper and the Supplementary Materials were prepared by both authors. F.T. gave critical revisions of the manuscript. **Competing interests:** The authors declare that they have no competing interests. **Data and materials availability:** All data needed to evaluate the conclusions in the paper are present in the paper and/or the Supplementary Materials. Additional data related to this paper may be requested from the authors.

Submitted 23 August 2017
Accepted 8 March 2018
Published 20 April 2018
10.1126/sciadv.aap7529

Citation: S. S. Krishtopenko, F. Teppe, Quantum spin Hall insulator with a large bandgap, Dirac fermions, and bilayer graphene analog. *Sci. Adv.* **4**, eaap7529 (2018).

Quantum spin Hall insulator with a large bandgap, Dirac fermions, and bilayer graphene analog

Sergey S. Krishtopenko and Frédéric Teppe

Sci Adv **4** (4), eaap7529.
DOI: 10.1126/sciadv.aap7529